Mapping local atomic structure of metallic glasses using machine learning aided 4D-STEM

Sangjun Kang [a,b], Vanessa Wollersen [a], Christian Minnert [c], Karsten Durst [c], Hyoung-Seop Kim [d,e,f], Christian Kübel [a,b,g,*], Xiaoke Mu [a,h,*]

[a] Institute of Nanotechnology (INT), Karlsruhe Institute of Technology (KIT), Eggenstein-Leopoldshafen 76344, Germany
[b] Joint Research Laboratory Nanomaterials, Technical University of Darmstadt (TUDa), Darmstadt, Germany
[c] Physical Metallurgy, Department of Materials Science, Technical University of Darmstadt (TUDa), Darmstadt 64287, Germany
[d] Department of Materials Science and Engineering, Pohang University of Science and Technology (POSTECH), Pohang 37673, Republic of Korea
[e] Advanced Institute for Materials Research (WPI-AIMR), Tohoku University, Sendai 980-8577, Japan
[f] Institute for Convergence Research and Education in Advanced Technology, Yonsei University, Seoul 03722, Republic of Korea
[g] Karlsruhe Nano Micro Facility (KNMFi), Karlsruhe Institute of Technology (KIT), Eggenstein-Leopoldshafen 76344, Germany
[h] School of Materials and Energy and Electron Microscopy Centre, Lanzhou University, Lanzhou 730000, China

Keywords:
Four dimensional-scanning transmission electron microscopy (4D-STEM)
Pair distribution function (PDF)
Nonnegative matrix factorization (NMF)
Metallic glasses

A B S T R A C T

Amorphous materials such as polymers, metallic and oxidic glasses consist of heterogeneous atomic/molecular packing at the nanoscale. Spatial variation of the local structure plays an important role in determining material properties. Experimentally probing the local atomic structure within the amorphous phase has been one of the main challenges for material research. Here, we present a new approach to characterize the local atomic structure and map structural variants in the amorphous phase using machine learning (ML) aided four dimensional-scanning transmission electron microscopy (4D-STEM). We utilized nonnegative matrix factorization (NMF) to identify the local structural types of metallic glasses in 4D-STEM datasets. Using Fe-based metallic glasses as a model system, we demonstrate that two basic structural types, one with a more liquid-like and another with a more solid-like structure, are distributed throughout the glass with a characteristic length scale of a few nanometers. Thermal annealing induces a change in their distribution and relative population but without the appearance of any additional phase. This provides new insights into the relaxation phenomena of metallic glasses and solid experimental evidence for the theoretical hypothesis on atomic packing in glassy structures.

1. Introduction

Metallic glasses are amorphous alloys which exhibit superior yield strength, wear resistance, and elastic limits compared to their crystalline counterparts. [1–3] The structure of metallic glasses can be described by the polyhedral packing of the constituting atoms. [4] The local atomic arrangement is not uniform everywhere due to packing frustration with different size ratios, chemical affinity, or negative heat of mixing between atomic species, but distinct types of structural motifs, *e.g.*, icosahedral cluster or other Zwischenkristall (Z) clusters, fill in the 3D volume. [5] Each structural motif exhibits certain geometrical and chemical features with various sharing/overlapping schemes resulting in different degrees of short-/medium-range order (S/MRO). [6–10] Metallic glasses are believed to exhibit a heterogeneous packing at the nanoscale, which can be simplified to consist of more stable (solid-like) and less stable (liquid-like) regions intermixed within the overall glassy matrix. [11] In general, the stable regions are characterized by efficient and dense polyhedral packing with minimal distortions, while the less stable region consists of unfavorable motifs with more free volumes. [12] The spatial variation of the local atomic structure has been a principal structural descriptor determining the material properties [13–18], and structural relaxation induced by quenching or thermal annealing has been a topic of interest because it leads a larger fraction of the stable regions and a better connection between them. [19–22]

Experimentally, numerous efforts have been devoted to characterize the local atomic structure of metallic glasses and to understand the structural evolution during thermal treatments. [16,19,23,24] Pair distribution function (PDF) analysis has been a powerful tool to describe

* Corresponding authors at: Institute of Nanotechnology (INT), Karlsruhe Institute of Technology (KIT), Eggenstein-Leopoldshafen 76344, Germany.
E-mail addresses: christian.kuebel@kit.edu (C. Kübel), muxk@lzu.edu.cn (X. Mu).

the atomic packing structure of metallic glasses. [19,25–27] PDF measures the relative atomic density as a function of pair distances, providing real-space information on the atomic structure of amorphous materials. [28–31] Dmowski et al. used PDF analysis based on neutron diffraction and observed an annihilation of free volume and local chemical ordering of the glass phase after annealing. [19] Their results provided a detailed view and experimental insight into the atomic structure of metallic glasses and how it changes upon relaxation. However, the large beam size employed in traditional scattering experiments results in an averaging of information from many local regions and thus cannot resolve the intrinsically heterogeneous nature of metallic glasses.

A solution has been to directly investigate nanosized volumes by electron diffraction using a semi-focused electron beam, *i.e.*, nano-beam electron diffraction (NBED). [11,32–34] NBED studies indicate that the nanoscale spatial heterogeneity is closely related to local structural variations involving different polyhedral structures. [11] Fluctuation electron microscopy (FEM), which measures the fluctuations of the diffraction intensity in NBED patterns at different probe positions, is used to gain an understanding of heterogeneous glass structures. [35–39] In ZrCu-based glasses, the FEM studies revealed that similar groups of atomic motifs agglomerate into nanometer-scaled regions resulting in spatial heterogeneity. [40] However, one difficulty of FEM has been that the results obtained in reciprocal space cannot directly be translated into real space structures. Many FEM studies, therefore, employed simulations, *e.g.*, molecular dynamics (MD) and reverse Monte Carlo (RMC), for reading out the information stored in reciprocal space. [40–43] Moreover, the NBED studies generally require very thin TEM specimens ($<$ 30 nm) for minimal overlap of diffraction features; otherwise, the result suffers from nonlinear degradation. [44]

Recently, scanning transmission electron microscopy-PDF analysis, so-called STEM-PDF, has been developed to characterize the local atomic packing structure of amorphous materials. [45,46] It uses a quasi-parallel electron probe to obtain the local PDFs using four-dimensional (4D)-STEM, thereby, enabling structural analysis and phase mapping at the nanoscale. [47] STEM-PDF analysis can be applied to much thicker samples compared to other advanced NBED analysis approaches such as FEM or local analysis of crystallographic rotational symmetry, [48] thus relaxing the sample preparation requirements. [49] However, the information from STEM-PDF is inevitably averaged over the anisotropic column in the projection direction giving rise to an overlap problem. Moreover, the finite collection angle of the electron diffraction patterns limits the resolution of the pair distribution peaks giving rise to difficulties in detecting subtle variations of the probed atomic structure. [50]

Multivariate statistical analysis (MSA), *e.g.*, principal component analysis (PCA) and independent component analysis (ICA), have been recently applied to solve the overlap problem and extract subtle signal variations in STEM-PDF datasets. [51,52] The results show the robustness of combining STEM-PDF and MSA techniques to reveal the atomic structure of amorphous materials at the nanoscale. However, PCA provides progressive approximations of the whole dataset and only recovers holistic representations, [53] while ICA assumes the hidden variables to be statistically independent and non-Gaussian distributed in the PCA results. [54,55] Due to the approximations, complex dependencies between hidden variables cannot be easily captured especially when the different atomic S/MROs possess similar partial features. Moreover, as PCA is based on linear combinations that generally involve complex cancellations of negative and positive numbers, an intuitive interpretation of resulting PDFs cannot be made in many cases. For these reasons, matrix factorization, which only allows additive combinations with non-negativity constraints, could be useful in analyzing STEM-PDF dataset and obtaining atomic configuration of individual structural types.

Here, we present an analytical method applied to STEM-PDF to study the local atomic structure of metallic glasses using nonnegative matrix factorization (NMF). We used a $Fe_{85.2}Si_{0.5}B_{9.5}P_4Cu_{0.8}$ (at.%) metallic glass ribbon as a model system, which receives attention owing to its soft ferromagnetism [56]. The new method identifies the structural bases of the glass phase without any preknowledge from atomic simulations. The resulting PDFs provide easily interpretable information about atomic packing of the individual structural bases forming the heterogeneous amorphous matrix. Our results reveal two structural types exhibiting more liquid-like and more solid-like characteristics, which are distributed at a length scale of a few nanometers. Interestingly, the average atomic configuration of the two structural types obtained from an as-spun sample does not change even after thermal annealing, indicating that the local structures persist during relaxation without giving rise to any new structural phases. Only their relative population and the spatial distribution substantially change due to annealing.

2. Experimental

2.1. Sample preparations

The $Fe_{85.2}Si_{0.5}B_{9.5}P_4Cu_{0.8}$ (at.%) metallic glass is prepared from the melt by rapid solidification onto rotating Cu wheels, resulting in a ribbon width of about 25 mm and a thickness of about 20 μm. [56] The as-spun glassy ribbon was flash-annealed for about 10 s at a temperature T_a = 633 K ($\sim$ 1.1 glass transition temperature). The annealing temperature was selected to match a previous study [56] which reported a significantly decreased fracture strain of the sample after the annealing. TEM lamellae from both as-spun and annealed ribbons were prepared by FIB (FEI Strata 400S). Thinning was performed to a sample thickness of about 50 nm for electron transparency with gradually decreasing acceleration voltage from 30 kV to 5 kV and beam currents from 8 nA to 2 pA to reduce the ion beam damage. The thicknesses of the FIB-prepared lamellae were measured by energy-filtered transmission electron microscopy (EFTEM) and confirmed to be about 50 nm for both samples using an estimated inelastic mean free path of 75 nm for electrons at an operation voltage of 300 kV and a mass density of 7.3 g/cm^3. [57]

2.2. Annular dark-field TEM and selected area electron diffraction

Conventional high-angle annular dark-field (HAADF)-STEM measurements were performed using an aberration-corrected Titan 80–300 (FEI Company) operated at a voltage of 300 kV with a 50 μm condenser C2 aperture, a camera length of 91 mm, and collection angle 70–200 mrad. Selected area electron diffraction (SAED) measurements were performed in TEM mode with parallel illumination using a camera length of 245 mm to determine the average PDFs of the as-spun and annealed metallic glasses.

2.3. 4D-STEM measurements and STEM-PDF analysis

4D-STEM experiments were performed using microprobe STEM mode with spot size 7, and a 30 μm C2 aperture resulting in a semi-convergence angle of 0.6 mrad. These settings result in a probe diameter of approximately 2 nm. A Merlin pixelated direct electron detector (Quantum Detector Ltd) was used to record the diffraction patterns with a camera length of 195 mm. 4D-STEM maps were acquired by capturing the diffraction patterns (256×256 pixels) with 4 ms exposure time for each pattern while scanning the electron probe over a 2D sample plane with a step size of 1.2 nm and a scan range of 128×128 pixels. Since the small convergence angle does not significantly degrade the angular resolution of the diffraction patterns (See Figure S1), they can be processed without deconvolution of the beam spread function. The diffraction patterns were integrated azimuthally to obtain radial profiles $I(q)$, where $q = 2\theta/\lambda$, θ is half of the scattering angle, and λ is the wavelength of the incident electrons. Note that we only considered the q values ranged within 0.25–1.6 Å^{-1} to avoid noise at large scattering angles, as shown in Fig. S1a. The structure factor is calculated by subtracting and normalizing with atomic scattering factors according to

$S(q) = \frac{I(q) \; N<f(q)^2>}{N\langle f(q)^2\rangle} q$, where N is the number of atoms within the volume sampled by the electron probe determined by matching $< f(q)^2 >$ at q_{max}, and $f(q)$ is the parameterized electron scattering factor for a single atom calculated based on X-ray reference data according to Ref. [58]. The equation $\langle f(q)\rangle = \sum_a C_a f_a(q)$ denotes an elemental average of the atomic scattering factor $f_a(q)$ over all elements, C_a presents in the atomic percentage of the a^{th} element. We assumed a uniform distribution of all elements in the sample for calculating the $S(q)$, which is in good agreement with EELS elemental maps for Fe and B (Figure S2), where no indication of elemental segregation was observed. The PDFs are obtained by a Fourier sine transformation of the structure factors according to the following equation: $\mathrm{PDF(r)} = \int_0^{q_{max}} S(q)\sin(2\pi qr)dq$.

In practice, the estimated $f(q)$ often does not perfectly match the experimental I(q) at small and large angles at the same time due to multiple elastic and inelastic scattering events. As amorphous materials do not have well-defined atomic columns, the scattering in an amorphous sample does not include any channeling. Instead, it results in multiple self-convolutions of the 2D kinetic diffraction pattern. [59] Therefore, multiple scattering in amorphous materials does not introduce any additional peaks or peak shifts but gives rise to a smooth background to the diffraction pattern. [51,60] A 4th-order polynomial function is subtracted from the structure factor to reduce contributions caused by plural and inelastic scattering as demonstrated in [61]. This significantly reduces artifacts caused by variations in thickness × atomic density in the samples [51]. To illustrate this effect explicitly, we performed PDF analysis of $Fe_{85.2}Si_{0.5}B_{9.5}P_4Cu_{0.8}$ metallic glass samples with different thicknesses in the range of 32 nm to 83 nm (Figure S3). Figure S3a-c shows that the corrected structure factors are (almost) the same, independent of sample thickness, and figure S3d shows nearly identical PDFs obtained from the samples of different thicknesses.

3. Results and discussion

3.1. Conventional TEM characterization

The as-spun and annealed $Fe_{85.2}Si_{0.5}B_{9.5}P_4Cu_{0.8}$ metallic glasses are inspected by conventional S/TEM analysis as shown in Fig. 1. STEM-HAADF images show inhomogeneous intensity fluctuations represented by dark and bright intensity contrasts. The intensity fluctuations are related to local structural variations, where dark and bright regions indicate lower and higher local density, respectively. The length scale of the fluctuation is about 5 nm and is evenly distributed in the as-spun sample (Fig. 1a). However, it is not an accurate measure of the size of the structural heterogeneity of the sample because the electron probes have finite sizes and only the averaged information along the beam propagation direction through the sample thickness can be obtained. Nevertheless, the length scale matches the previous TEM study on metallic glasses [32]. Note that the intensity fluctuations become substantially reduced after annealing treatment (Fig. 1c). This indicates a reduced structural heterogeneity considering that the thicknesses of the as-spun and annealed samples were similar (~ 50 ± 5 nm). The SAED diffraction patterns show the amorphous nature for both samples (Fig. 1b and d). PDFs are calculated from the SAED patterns to compare the average atomic configuration in the as-spun and annealed samples (Fig. 1e). Although quantitative analysis of electron pair correlation value itself is not easy due to different multiple scattering contributions from the samples, the shift of PDF peak position can still be reliably determined via proper normalization by the intensity of the first peak. It can be seen that the first peak of the PDF (2.51 Å for as-spun and 2.49 Å

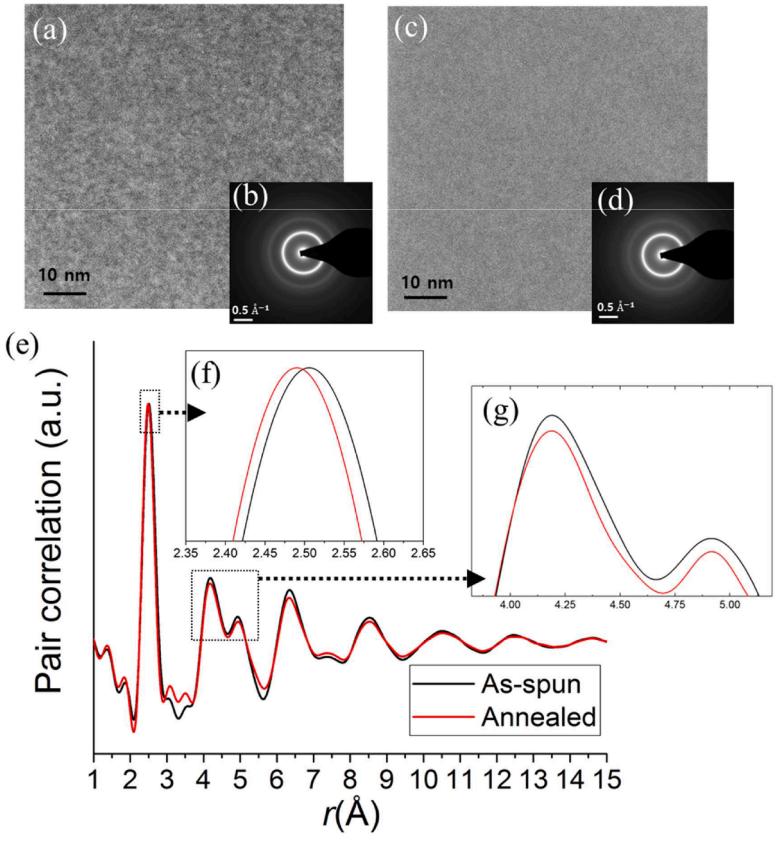

Fig. 1. Conventional S/TEM investigation of as-spun and annealed $Fe_{85.2}Si_{0.5}B_{9.5}P_4Cu_{0.8}$ metallic glasses. (a) A STEM-HAADF image and (b) SEAD pattern for the as-spun glass, and (c) a STEM-HAADF image and (d) SEAD pattern for the annealed glass. (e) PDFs calculated from the SEAD patterns of the as-spun and annealed glasses. The heights of the PDFs are normalized by their first peak to highlight the peak shifts.

for annealed samples) is shifted to a shorter atomic distance, indicating structural densification after annealing treatment. No significant differences in the peaks at high *r* are observed between samples, revealing that major structural change only happened in the short/medium range during the annealing.

3.2. 4D-STEM and machine learning aid STEM-PDF

For local structural analysis, the 4D-STEM datasets were converted to PDF cubes and analyzed using an NMF algorithm as shown in Fig. 2. To model the signal mixing, the STEM-PDF data cube is represented by a 2D matrix $\boldsymbol{V}$, where the rows are PDFs at nth columnar locations ($\boldsymbol{V}_n$) and the columns correspond to the atomic pair distance. Ideally, the experimental PDFs can be considered as a linear combination of PDFs from the structural bases, *i.e.*, basis PDFs as demonstrated in [45]. The mixed signal can then be modeled by a matrix factorization $\boldsymbol{V} = \boldsymbol{WH}$, where the rows of the matrix $\boldsymbol{H}$ represent the basis PDFs and $\boldsymbol{W}$ is a weighting matrix describing the contributions of $\boldsymbol{H}$ mixed in $\boldsymbol{V}$. The NMF algorithm deconvolutes $\boldsymbol{H}$ and $\boldsymbol{W}$ without any preknowledge of the structural bases. NMF is distinguished from other learning methods by its non-negativity constraints for the matrix factors. [55] To meet these constraints, in our work, $\boldsymbol{V}$ was shifted to be positive by adding the global minimum before applying the algorithm. The exact height of $\boldsymbol{V}$ is not crucial for the success of NMF in identifying the basis PDFs because the information in the PDFs is contained in the oscillations of the signals, not in the constant offset. The non-negativity constraint only permits additions during matrix factorization. This is compatible with the notion of a neural network where neuron connectivity and synaptic strength cannot be negative and thus able to recover the individual structure of basis motifs providing a part-based representation (Fig. 2b, top). [55]

In this work, we used the low-rank approximate NMF algorithms implemented in Matlab. [62] The algorithm finds an approximate factorization $\boldsymbol{WH}$ using iterative update rules for nonnegative $\boldsymbol{V}$. A two-step NMF calculation is applied to the STEM-PDF dataset to ensure a unique and accurate solution, targeting three principal factors (aiming for two different glassy configurations and a residual signal). The first NMF calculation roughly searches for the global minimum as a unique solution with low termination tolerance for the residual signal with up to five iterations, leading to good starting points $\boldsymbol{W}_0$ and $\boldsymbol{H}_0$ for the next calculation. In the second step, NMF starts from the initial $\boldsymbol{W}_0$ and $\boldsymbol{H}_0$ and calculates an accurate solution with 0.00001 % termination tolerance for the residual signal and up to 1000 iterations. To check the reliability of our method, we performed additional PDF and NMF analysis for the as-spun sample at a different sample location where the sample thickness is different using the same microscopy settings (Figure S4). The results were qualitatively the same, proving the reproducibility of the NMF-aided STEM-PDF analysis.

3.3. Mapping local atomic structures of metallic glass

Fig. 3 shows NMF results for a STEM-PDF dataset. The basis PDFs represent the average atomic configuration for each structural type, which may consist of various atomic motifs and different connection schemes. Structural types 1 and 2 show typical PDF patterns of the S/MRO structure of an amorphous material. Note that Structural type 3 only shows wave-like fluctuations with a significantly reduced correlation amplitude compared to other PDFs. Such simple fluctuations are also observed in PCA analysis for low-ranked information which can be considered to be background noise. [63] Structural types 1 and 2 can be clearly distinguished by their first and second peaks. The first peak position of Structural type 1 corresponds to a larger atomic distance of 2.53 Å compared to Structural type 2 at 2.46 Å. The first peak of Structural type 2 is substantially higher and shaper than that of Structural type 1, *e.g.*, their full width at half maximum (FWHM) are 0.65 Å (Structural type 1) and 0.48 Å (Structural type 2), respectively. This observation indicates that Structural type 2 possesses denser (with higher coordination number) and well-defined nearest neighbors than Structural type 1. In line with the first peak information, the second peak of Structural type 2 (4.10 Å) is located at a shorter atomic distance compared to that of Structural type 1 (4.24 Å), indicating that Structural type 2 exhibits a denser structure even in the second nearest neighbor arrangement. Notably, the second peaks of both types appear with a shoulder peak at a higher atomic distance. Since the polyhedral clusters forming the metallic glasses share different numbers of atoms to overcome packing frustration, relating the positions of the shoulder peak with the number of shared atoms can offer insights into cluster connectivity and the resulting degrees of MRO. [6,64-66] For polyhedra connections corresponding to 1 atom, 2 atoms, and 3 atoms, the most probable distance for 2nd peaks can be estimated to be $2R_1$ (5.05 Å for type 1 and 4.92 Å for type 2), $\sqrt{3}R_1$ (4.38 Å for type 1 and 4.26 Å for type 2), and $\sqrt{\frac{8}{3}}R_1$

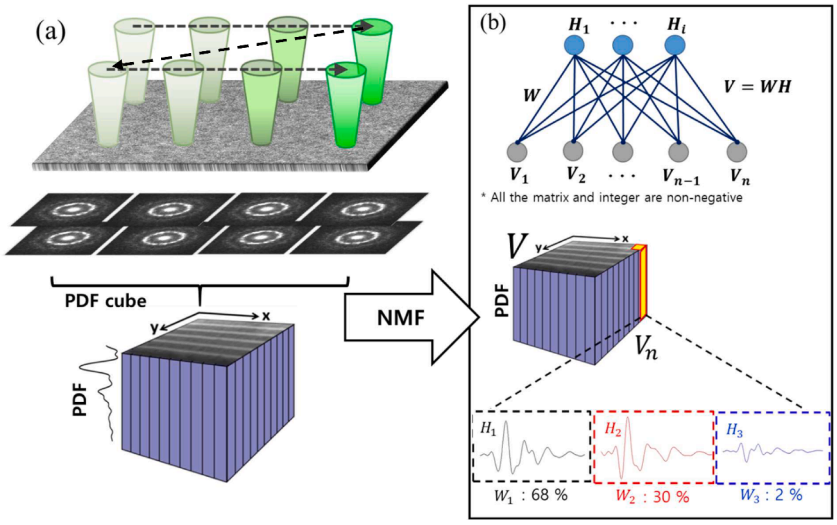

Fig. 2. (a) Schematic illustration of NMF-aided STEM-PDF analysis. (b) Probabilistic blind source model underlying non-negative matrix factorization. The diagram model depicts a network in which experimental $\boldsymbol{V_n}$ are in the bottom layer of nodes and the blind sources $\boldsymbol{H_i}$in the top layer of nodes (top). The experimental $\boldsymbol{V}$ can be represented by probability distribution with $V_n \quad \sum_1^i W_{n,i} H_i$. According to the model, the significance of sources $\boldsymbol{H_i}$on $\boldsymbol{V}$ is represented by a connection with the weight matrix $W_{n,i}$. In the application to STEM-PDF cube, an experimental PDF V_n is decomposed by basis PDFs $\boldsymbol{H_1}$, $\boldsymbol{H_2}$,and $\boldsymbol{H_3}$ with their weighing constant $\boldsymbol{W_1}$, $\boldsymbol{W_2}$, and $\boldsymbol{W_3}$.

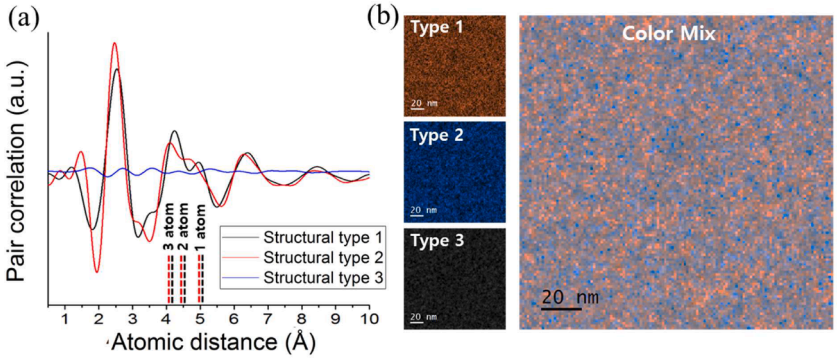

Fig. 3. NMF results for a STEM-PDF dataset of the as-spun $Fe_{85.2}Si_{0.5}B_{9.5}P_4Cu_{0.8}$ metallic glass. (a) Obtained basis PDFs. The vertical dash lines indicate the distances of the polyhedra connections with different numbers of shared atoms (ranging from 1 to 3) for structural type 1 (black), structural type 2 (read) (b) Spatial distribution of the basic structural types indicated by different colors. The brightness indicates their population. All three maps are incorporated in the color mix map at the rightmost.

(4.13 Å for type 1 and 4.02 Å for type 2), respectively, where R_1 is the first peak position of each motif. [67,68] The estimated distances for the polyhedra connections with the number of shared atoms are marked by dashed lines for both structural types in Fig. 3a. The main branch of the second peak appears at $\sqrt{\frac{8}{3}}R_1$ for both structural types, indicating that the structural types are dominated by polyhedra connected by sharing three atoms. Interestingly, their subpeaks appearing at larger pair distances show a meaningful difference between the two types. The subpeak of type 1 is located at a relatively large atomic distance (4.95 Å) which corresponds to vertex-connections (single atom shared between clusters). In contrast, the position of the shoulder peak of structural type 2 (4.66 Å) indicates that the edge-connection (two atom shared between clusters) dominates here. Since the number of shared atoms in the polyhedral connections increases when the medium-range packing efficiency of the system becomes higher. [6,69] This means that structural type 2 exhibits a higher packing efficiency in the SRO and MRO consisting of more energetically stable motifs, *i.e.*, geometrically favored motif (GFM), compared to structural type 1 possessing more geometrically unfavored motifs (GUM) (See Figure S5). [70] Following the commonly used description in simulations, we will refer to structural type 1 as "liquid-like" and structural type 2 as "solid-like." [4]

The spatial distribution of each structural type is shown in Fig. 2b. Note that we regarded Structural type 3 as noise and excluded it from further analysis. The correlative length of each structural type is measured by an autocorrelation analysis of the maps. The size of the local zones is 5.43 nm for the liquid-like region and 5.66 nm for the solid-like region, which is in good agreement with previous observations obtained from nanobeam diffraction and simulations. [11,32,71,72]

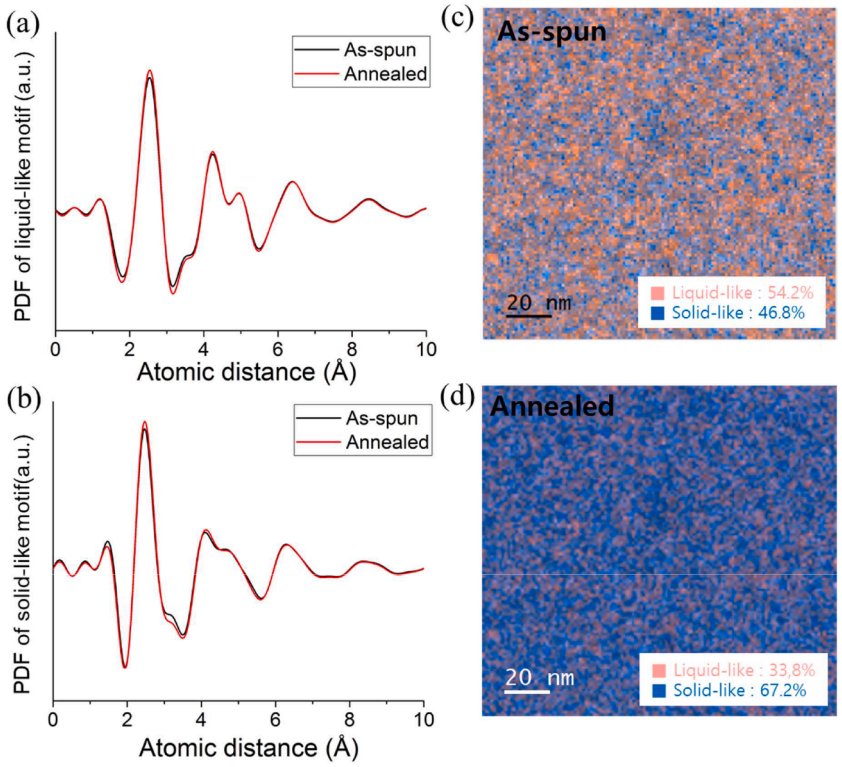

Fig. 4. Atomic structure mapping of the as-spun and annealed $Fe_{85.2}Si_{0.5}B_{9.5}P_4Cu_{0.8}$ metallic glasses using NMF-aided STEM-PDF. Basis PDFs of (a) the liquid-like and (b) the solid-like structural bases separately obtained from both as-spun and annealed metallic glass samples. Maps of the liquid-like and solid-like structural bases for (c) as-spun and (d) annealed samples with the fraction of each structural type shown in a white box.

3.4. Influence of annealing treatment on atomic structure and spatial distribution of structural bases

Fig. 4 compares the PDFs for the liquid-like and solid-like structural bases of the as-spun and annealed $Fe_{85.2}Si_{0.5}B_{9.5}P_4Cu_{0.8}$ metallic glasses and their spatial distribution. The PDFs for the liquid-like and solid-like structural bases, which have been obtained fully independently for the two different samples, are in excellent agreement with each other except for slight peak height deviations (Fig. 4a and b). This agreement proves the reliability and validity of the method. More importantly, the result reveals that both as-spun and annealed samples possess the same basic structural types with nearly identical atomic configurations. This indicates that the basic configuration of each structural type persists during relaxation. This observation matches MD simulations, which characterized the glass motifs into two groups of basis motifs, *i.e.* GFM and GUM. [15,73] We further quantify their relative contribution and the spatial distribution in both as-spun and annealed samples using multi-linear least square fitting (MLLS). We found that the annealing treatment effectively changes the concentration and spatial distribution of the structural bases. The difference can be seen in Fig. 4c and d, where the concentration of the solid-like regions significantly increases from 46.8% (as-spun sample) to 67.2% (annealed sample). This experimental observation supports the theoretical hypothesis that the relaxation process at near glass transition temperature leads to a larger fraction of the stable structural type with the annihilation of excessive free volume. [20–22]

4. Conclusions

We provide a new approach for characterizing the local atomic packing and mapping their distribution in a metallic glass using ML-aided 4D-STEM analysis. We utilize NMF for blind source separation of STEM-PDF datasets. Unlike other learning algorithms, such as PCA, NMF provides a part-based representation resulting in more intuitively interpretable information about the structural bases of metallic glasses. In this work, we experimentally characterize the local atomic configuration and map their distribution in metallic glasses. The results indicate the presence of two basic glassy structures corresponding to more liquid-like and more solid-like structures, distributed at a length scale of a few nanometers in as-spun and annealed $Fe_{85.2}Si_{0.5}B_{9.5}P_4Cu_{0.8}$ metallic glasses. The PDF analysis shows that the two fundamental glassy structures in both the as-spun and annealed glasses are essentially the same, signifying a uniform atomic arrangement in both states. This implies that their structural integrity remains unchanged during relaxation. However, their relative population and distribution substantially change during annealing but without the emergence of additional structural types. This observation enhances our understanding of the relaxation phenomena in metallic glasses and contributes to a refined comprehension of their structural evolution.

Author contributions

S.J.K and X.M developed the methods and performed the TEM experiments. K.D and C.M provided the Fe-based sample. S.J.K, H.S.K, X. M, D.W, and C.K analyzed data. All authors discussed the results. X.M and C.K supervised the project. S.J.K, X.M, and C.K wrote the manuscript. All authors contributed to the revision of the manuscript.

Data availability

The data that support the findings of this study are openly available in KITOpen at https://doi.org/10.35097/1802, reference number 1000164027.

Declaration of Competing Interest

The authors declare that they have no known competing financial interests or personal relationships that could have appeared to influence the work reported in this paper.

Acknowledgments

The authors are grateful to the Karlsruhe Nano Micro Facility (KNMFi) for support and access to FIB and TEM facilities. X. M. acknowledges the financial support received from Deutsche Forschungsgemeinschaft's (DFG) funding (MU 4276/1–1). The authors would like to express their sincere gratitude to Professor Yongsoo Yang and Dr. Juhyeok Lee for their insightful discussion, which helped to shape the research methodology and refine the analysis.

References

[1] A.L. Greer, Metallic glasses, Science 267 (5206) (1995) 1947–1953.
[2] M. Telford, The case for bulk metallic glass, Mater. Today 7 (3) (2004) 36–43.
[3] C.A. Schuh, T.C. Hufnagel, U. Ramamurty, Mechanical behavior of amorphous alloys, Acta Mater. 55 (12) (2007) 4067–4109.
[4] Y. Cheng, E. Ma, Atomic-level structure and structure–property relationship in metallic glasses, Prog. Mater. Sci. 56 (4) (2011) 379–473.
[5] K. Laws, D. Miracle, M. Ferry, A predictive structural model for bulk metallic glasses, Nat. Commun. 6 (1) (2015) 8123.
[6] H. Sheng, W. Luo, F. Alamgir, J. Bai, E. Ma, Atomic packing and short-to-medium-range order in metallic glasses, Nature 439 (7075) (2006) 419–425.
[7] Z. Li, Z. Huang, F. Sun, X. Li, J. Ma, Forming of metallic glasses: mechanisms and processes, Mater. Today Adv. 7 (2020), 100077.
[8] T. Egami, C.W. Ryu, World beyond the nearest neighbors, J. Phys. Condens. Matter 35 (17) (2023), 174002.
[9] Y. Cheng, E. Ma, H. Sheng, Atomic level structure in multicomponent bulk metallic glass, Phys. Rev. Lett. 102 (24) (2009), 245501.
[10] D.B. Miracle, T. Egami, K.M. Flores, K.F. Kelton, Structural aspects of metallic glasses, Mrs Bull. 32 (8) (2007) 629–634.
[11] F. Zhu, A. Hirata, P. Liu, S. Song, Y. Tian, J. Han, T. Fujita, M. Chen, Correlation between local structure order and spatial heterogeneity in a metallic glass, Phys. Rev. Lett. 119 (21) (2017), 215501.
[12] T. Egami, V. Vitek, Local structural fluctuations and defects in metallic glasses, J. Non Cryst. Solids 61 (1984) 499–510.
[13] D.S. Wilkinson, W. Pompe, M. Oeschner, Modeling the mechanical behaviour of heterogeneous multi-phase materials, Prog. Mater. Sci. 46 (3–4) (2001) 379–405.
[14] C. Liu, R. Maaß, Elastic fluctuations and structural heterogeneities in metallic glasses, Adv. Funct. Mater. 28 (30) (2018), 1800388.
[15] E. Ma, J. Ding, Tailoring structural inhomogeneities in metallic glasses to enable tensile ductility at room temperature, Mater. Today 19 (10) (2016) 568–579.
[16] Y. Waseda, T. Egami, Effect of low-temperature annealing and deformation on the structure of metallic glasses by X-ray diffraction, J. Mater. Sci. 14 (1979) 1249–1253.
[17] T. Egami, Understanding the properties and structure of metallic glasses at the atomic level, JOM 62 (2) (2010) 70–75.
[18] F. Zhu, S. Song, K.M. Reddy, A. Hirata, M. Chen, Spatial heterogeneity as the structure feature for structure–property relationship of metallic glasses, Nat. Commun. 9 (1) (2018) 3965.
[19] W. Dmowski, C. Fan, M. Morrison, P. Liaw, T. Egami, Structural changes in bulk metallic glass after annealing below the glass-transition temperature, Mater. Sci. Eng. A 471 (1–2) (2007) 125–129.
[20] Y. Fan, T. Iwashita, T. Egami, Evolution of elastic heterogeneity during aging in metallic glasses, Phys. Rev. E 89 (6) (2014), 062313.
[21] F. Zhu, H. Nguyen, S. Song, D.P. Aji, A. Hirata, H. Wang, K. Nakajima, M. Chen, Intrinsic correlation between β-relaxation and spatial heterogeneity in a metallic glass, Nat. Commun. 7 (1) (2016) 11516.
[22] H.B. Yu, W.H. Wang, K. Samwer, The β relaxation in metallic glasses: an overview, Mater. Today 16 (5) (2013) 183–191.
[23] Y. Liu, T. Fujita, D. Aji, M. Matsuura, M. Chen, Structural origins of Johari-Goldstein relaxation in a metallic glass, Nat. Commun. 5 (1) (2014) 3238.
[24] W.H. Wang, Dynamic relaxations and relaxation-property relationships in metallic glasses, Prog. Mater. Sci. 106 (2019), 100561.
[25] P. Lamparter, A. Habenschuss, A.H. Narten, Neutron and X-ray diffraction study of the Ti84Si16 metallic glass, J. Non Cryst. Solids 86 (1) (1986) 109–120.
[26] B. Sarac, A. Bernasconi, J. Wright, M. Stoica, F. Spieckermann, M. Mühlbacher, J. Keckes, X. Bian, G. Wang, J. Eckert, Structural modifications in sub-Tg annealed CuZr-based metallic glass, Mater. Sci. Eng. A 707 (2017) 245–252.

[27] M.L. Morrison, W. Dmowski, T.W. Wilson, P.K. Liaw, C.T. Liu, J.W. Richardson, W. D. Porter, Pair distribution function analyses of structural relaxation in a Zr-Based bulk metallic glass, MRS Online Proceedings Library (OPL) 840 (2004) Q1–5.
[28] P. Egelstaff, An Introduction to the Liquid State, Elsevier, 2012.
[29] T. Egami, Structural relaxation in amorphous Fe40Ni40P14 B6 studied by energy dispersive X-ray diffraction, J. Mater. Sci. 13 (12) (1978) 2587–2599.
[30] Y. Suzuki, J. Haimovich, T. Egami, Bond-orientational anisotropy in metallic glasses observed by x-ray diffraction, Phys. Rev. B 35 (5) (1987) 2162.
[31] B.E. Warren, X-ray Diffraction, Courier Corporation, 1990.
[32] F. Zhu, S. Song, K.M. Reddy, A. Hirata, M. Chen, Spatial heterogeneity as the structure feature for structure–property relationship of metallic glasses, Nat. Commun. 9 (1) (2018) 1–7.
[33] A. Hirata, P. Guan, T. Fujita, Y. Hirotsu, A. Inoue, A.R. Yavari, T. Sakurai, M. Chen, Direct observation of local atomic order in a metallic glass, Nat. Mater. 10 (1) (2011) 28–33.
[34] J. Hwang, Z. Melgarejo, Y.E. Kalay, I. Kalay, M.J. Kramer, D. Stone, P. Voyles, Nanoscale structure and structural relaxation in Zr 50 Cu 45 Al 5 bulk metallic glass, Phys. Rev. Lett. 108 (19) (2012), 195505.
[35] M. Treacy, J. Gibson, L. Fan, D. Paterson, I. McNulty, Fluctuation microscopy: a probe of medium range order, Rep. Prog. Phys. 68 (12) (2005) 2899.
[36] J. Hwang, P. Voyles, Variable resolution fluctuation electron microscopy on Cu-Zr metallic glass using a wide range of coherent STEM probe size, Microsc. Microanal. 17 (1) (2011) 67–74.
[37] P. Voyles, J. Hwang, Fluctuation electron microscopy, Charact. Mater. (2002) 1–7.
[38] J.M. Gibson, M.M.J. Treacy, P.M. Voyles, Atom pair persistence in disordered materials from fluctuation microscopy, Ultramicroscopy 83 (3) (2000) 169–178.
[39] P.M. Voyles, J.R. Abelson, Medium-range order in amorphous silicon measured by fluctuation electron microscopy, Sol. Energy Mater. Sol. Cells 78 (1) (2003) 85–113.
[40] J. Hwang, Z.H. Melgarejo, Y.E. Kalay, I. Kalay, M.J. Kramer, D.S. Stone, P. M. Voyles, Nanoscale structure and structural relaxation in Zr50Cu45A5 bulk metallic glass, Phys. Rev. Lett. 108 (19) (2012), 195505.
[41] S.N. Bogle, P.M. Voyles, S.V. Khare, J.R. Abelson, Quantifying nanoscale order in amorphous materials: simulating fluctuation electron microscopy of amorphous silicon, J. Phys. Condens. Matter 19 (45) (2007), 455204.
[42] J.J. Maldonis, J. Hwang, P.M. Voyles, H.R.M.C. FEMSIM+, Simulation of and structural refinement using fluctuation electron microscopy for amorphous materials, Comput. Phys. Commun. 213 (2017) 217–222.
[43] J. Wen, Y. Cheng, J. Wang, E. Ma, Distinguishing medium-range order in metallic glasses using fluctuation electron microscopy: a theoretical study using atomic models, J. Appl. Phys. 105 (4) (2009), 043519.
[44] F. Yi, P.M. Voyles, Effect of sample thickness, energy filtering, and probe coherence on fluctuation electron microscopy experiments, Ultramicroscopy 111 (8) (2011) 1375–1380.
[45] X. Mu, A. Mazilkin, C. Sprau, A. Colsmann, C. Kübel, Mapping structure and morphology of amorphous organic thin films by 4D-STEM pair distribution function analysis, Microscopy 68 (4) (2019) 301–309.
[46] X. Mu, S. Neelamraju, W. Sigle, C.T. Koch, N. Toto, J.C. Schön, A. Bach, D. Fischer, M. Jansen, P.A. van Aken, Evolution of order in amorphous-to-crystalline phase transformation of MgF2, J. Appl. Crystallogr. 46 (4) (2013) 1105–1116.
[47] C. Ophus, Four-dimensional scanning transmission electron microscopy (4D-STEM): from scanning nanodiffraction to ptychography and beyond, Microsc. Microanal. 25 (3) (2019) 563–582.
[48] A. Hirata, L.J. Kang, T. Fujita, B. Klumov, K. Matsue, M. Kotani, A.R. Yavari, M. W. Chen, Geometric frustration of icosahedron in metallic glasses, Science 341 (6144) (2013) 376–379.
[49] S. Kang, D. Wang, A. Caron, C. Minnert, K. Durst, C. Kübel, X. Mu, Direct observation of quadrupolar strain fields surrounding Eshelby inclusions in metallic glasses, Adv. Mater. (2023), 2212086.
[50] B. Toby, T. Egami, Accuracy of pair distribution function analysis applied to crystalline and non-crystalline materials, Acta Crystallogr. A Found. Crystallogr. 48 (3) (1992) 336–346.
[51] X. Mu, L. Chen, R. Mikut, H. Hahn, C. Kübel, Unveiling local atomic bonding and packing of amorphous nanophases via independent component analysis facilitated pair distribution function, Acta Mater. 212 (2021), 116932.
[52] X. Mu, M.R. Chellali, E. Boltynjuk, D. Gunderov, R.Z. Valiev, H. Hahn, C. Kübel, Y. Ivanisenko, L. Velasco, Unveiling the local atomic arrangements in the shear band regions of metallic glass, Adv. Mater. 33 (12) (2021), 2007267.
[53] H.K. Kim, H.Y. Ha, J.H. Bae, M.K. Cho, J. Kim, J. Han, J.Y. Suh, G.H. Kim, T.H. Lee, J.H. Jang, Nanoscale light element identification using machine learning aided STEM-EDS, Sci. Rep. 10 (1) (2020) 1–12.
[54] I.T. Jolliffe, J. Cadima, Principal component analysis: a review and recent developments, Philos. Trans. R. Soc. Math. Phys. Eng. Sci. 374 (2065) (2016), 20150202.
[55] D.D. Lee, H.S. Seung, Learning the parts of objects by non-negative matrix factorization, Nature 401 (6755) (1999) 788–791.
[56] C. Minnert, M. Kuhnt, S. Bruns, A. Marshal, K.G. Pradeep, M. Marsilius, E. Bruder, K. Durst, Study on the embrittlement of flash annealed Fe85.2B9.5P4Cu0.8Si0.5 metallic glass ribbons, Mater. Des. 156 (2018) 252–261.
[57] T. Malis, S. Cheng, R. Egerton, EELS log-ratio technique for specimen-thickness measurement in the TEM, J. Electron Microsc. Tech. 8 (2) (1988) 193–200.
[58] Earl J. Kirkland, Advanced computing in electron microscopy, 12, Plenum Press, New York, 1998.
[59] G.R. Anstis, Z. Liu, M. Lake, Investigation of amorphous materials by electron diffraction — The effects of multiple scattering, Ultramicroscopy 26 (1) (1988) 65–69.
[60] J. Ankele, J. Mayer, P. Lamparter, S. Steeb, Quantitative electron diffraction data of amorphous materials, Z. Naturforsch. A 60 (6) (2005) 459–468.
[61] X. Mu, D. Wang, T. Feng, C. Kübel, Radial distribution function imaging by STEM diffraction: phase mapping and analysis of heterogeneous nanostructured glasses, Ultramicroscopy 168 (2016) 1–6.
[62] M.W. Berry, M. Browne, A.N. Langville, V.P. Pauca, R.J. Plemmons, Algorithms and applications for approximate nonnegative matrix factorization, Comput. Stat. Data Anal. 52 (1) (2007) 155–173.
[63] X. Mu, L. Chen, R. Mikut, H. Hahn, C. Kübel, Unveiling local atomic bonding and packing of amorphous nanophases via independent component analysis facilitated pair distribution function, Acta Mater. 212 (2021).
[64] Q. Yu, X. Wang, H. Lou, Q. Cao, J. Jiang, Atomic packing in Fe-based metallic glasses, Acta Mater. 102 (2016) 116–124.
[65] J. Ding, E. Ma, M. Asta, R.O. Ritchie, Second-nearest-neighbor correlations from connection of atomic packing motifs in metallic glasses and liquids, Sci. Rep. 5 (1) (2015) 17429.
[66] W. Luo, H. Sheng, E. Ma, Pair correlation functions and structural building schemes in amorphous alloys, Appl. Phys. Lett. 89 (13) (2006), 131927.
[67] Y.C. Liang, R.S. Liu, Y.F. Mo, H.R. Liu, Z.A. Tian, Q.-y. Zhou, H.T. Zhang, L.L. Zhou, Z.Y. Hou, P. Peng, Influence of icosahedral order on the second peak splitting of pair distribution function for Mg70Zn30 metallic glass, J. Alloys Compd. 597
(2014) 269–274.
[68] S. Pan, J. Qin, W. Wang, T. Gu, Origin of splitting of the second peak in the pair-distribution function for metallic glasses, Phys. Rev. B 84 (9) (2011), 092201.
[69] J. Ding, E. Ma, M. Asta, R.O. Ritchie, Second-nearest-neighbor correlations from connection of atomic packing motifs in metallic glasses and liquids, Sci. Rep. 5 (1) (2015) 1–9.
[70] E. Ma, Tuning order in disorder, Nat. Mater. 14 (6) (2015) 547–552.
[71] S. Im, Z. Chen, J.M. Johnson, P. Zhao, G.H. Yoo, E.S. Park, Y. Wang, D.A. Muller, J. Hwang, Direct determination of structural heterogeneity in metallic glasses using four-dimensional scanning transmission electron microscopy, Ultramicroscopy 195 (2018) 189–193.
[72] F. Zhu, S. Song, K.M. Reddy, A. Hirata, M. Chen, Spatial heterogeneity as the structure feature for structure-property relationship of metallic glasses, Nat. Commun. 9 (1) (2018) 3965.
[73] J. Ding, S. Patinet, M.L. Falk, Y. Cheng, E. Ma, Soft spots and their structural signature in a metallic glass, Proc. Natl. Acad. Sci. 111 (39) (2014) 14052–14056.